SIMULATIONS OF A HIGH-RESOLUTION MICRO-PET SYSTEM BASED ON LIQUID XENON

by

CHARLES MCCONNELL CLEMENTS

B.Sc., The University of Alberta, 2011

A THESIS SUBMITTED IN PARTIAL FULFILLMENT OF
THE REQUIREMENTS FOR THE DEGREE OF

MASTER OF SCIENCE

in

THE FACULTY OF GRADUATE STUDIES

(Physics)

THE UNIVERSITY OF BRITISH COLUMBIA

(Vancouver)

September 2011

Supervisor: Professor Douglas Bryman

Abstract

The capabilities and system performance of a high-resolution micro-PET system based on liquid xenon have been studied. Monte-Carlo simulations of scintillation events within a single sector of a twelve-sector prototype have been performed, and the results have been analyzed using Neural Network algorithms. The ability of the system to distinguish interaction points using scintillation information has been analyzed and presented. Monte-Carlo simulations of a full scale prototype have also been performed using NEMA standard mouse and rat phantoms. A novel scatter suppression scheme based on weighted Line of Response data is presented, and the effects on scatter fraction and background noise are analyzed.

Table of Contents

List of Tables

List of Figures

Acknowledgements

I would like to thank my supervisor, Professor Doug Bryman, for his help and support through my studies, and for his encouragement to experiment with new ideas. His insights and suggestions were an invaluable part of my research.

I would also like to acknowledge Alice Miceli for her countless help and suggestions. Much of this work would not have been possible without her help with Geant4 code and her constant willingness and ability to solve problems.

Many thanks to my colleagues at TRIUMF and at UBC, also to the TRIUMF support staff and administration for making my experience as enjoyable and stimulating as possible.

Special thanks as well to the course instructors at UBC and BCCA, especially Prof.'s Cheryl Duzenli and Alex Mackay for their help and encouragement and for the organization of an outstanding Medical Physics program.

Dedication

I would like to dedicate this work to my loving wife Jorie. Her support and encouragement are a source of inspiration to my life. Thank you for always helping me pursue my dreams, and for always being there for me. I would also like to dedicate this to my little boy Bryson, who never failed to cheer me up after long days and motivated me to be a better person.

Chapter 1: Introduction

Most modern medical imaging techniques can be categorized into two functions: anatomical imaging, and functional or metabolic imaging. Anatomical imaging uses various techniques to map physical structures and anatomical features. Functional imaging is used to identify and map biological or metabolic processes within the subject. Modern physicians often use a combination of anatomic and functional imaging to be able to accurately diagnose disease and prescribe treatment. One method of functional imaging of growing importance is Positron Emission Tomography (PET). Research in PET systems continues to make improvements in image quality; however, conventional PET scanners are limited in contrast, spatial resolution, and sensitivity by limitations in the scanner hardware. The Liquid Xenon PET (LXePET) project seeks to address current limitations in image resolution, sensitivity, and signal-to-noise ratio, by reducing detector limitations down to the essential physical limitations of positron range and non-colinearity. This thesis will examine some of the current challenges in PET imaging, and show how the LXePET scanner is attempting to address them. Simulations of the LXePET detector prototype performance will be presented, along with techniques for identifying interaction locations within the detector. Finally, a method for improving image quality through a chi-squared weighted sinogram will be discussed.

Introduction to PET

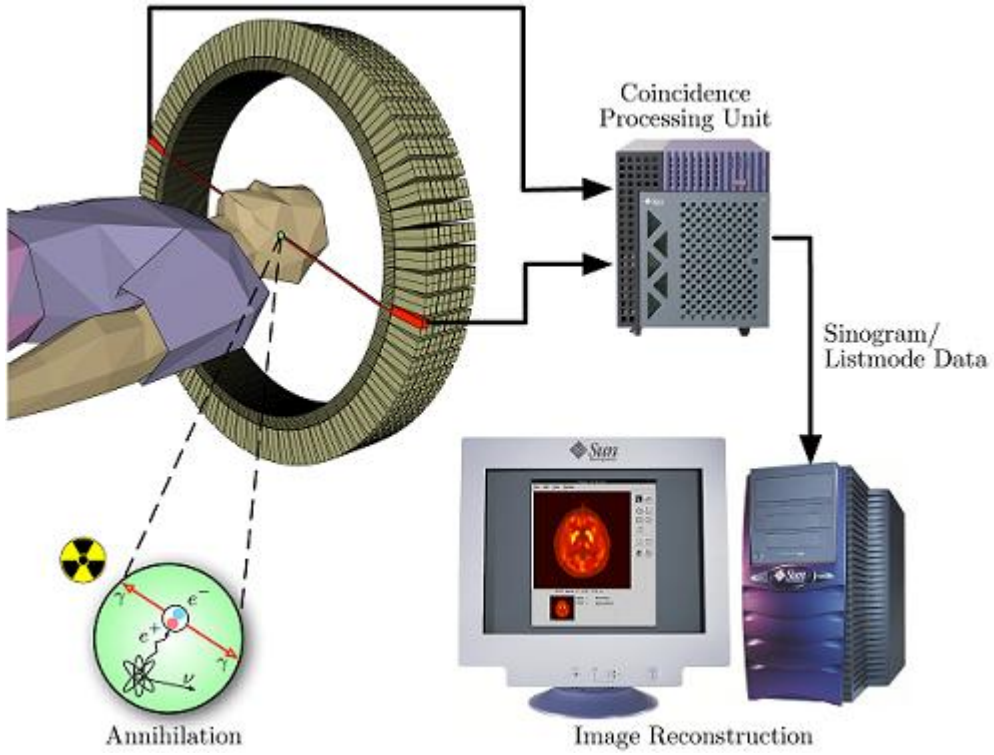

Figure 1: Schematic representation of the principle of PET systems. Positron annihilation results in two collinear gamma photons which are detected in coincidence in the detector. Image used under GPL from (1).

Positron Emission Tomography (PET) is a diagnostic medical imaging modality that uses radioactively labelled pharmaceuticals (tracers) to generate images of functional and metabolic processes. These tracers, such as 18F-fluorodeoxyglucose (FDG), containing positron emitting radioisotopes are injected into a patient and travel through the circulatory system where they are taken up by various organs and tissues.

PET images rely on both the ability of drug or tracer to target a specific tissue, and the ability of the detector to identify the source of emission of the positrons, thus identifying the location of the tracer. Emitted positrons quickly annihilate with nearby electrons, creating two collinear, orthogonally polarized, gamma photons with energy of the rest mass energy of the electron (511 keV). These photons are detected in coincidence by the PET detector, which generally consists of a ring of scintillation crystals or similar material. Two coincident detections of

annihilation photons allows the formation of a line of response (LOR) through which the source of the annihilation is calculated. PET images are generated by reconstructing LORs from millions of annihilations within the subject into an image representing the source distribution of the radioactive tracer. By identifying the uptake of the tracer into various tissues, researchers and physicians can gain insights into biological processes and abnormalities. PET scans have a wide variety of applications, including cardiology, neurology and cognitive neuroscience, oncology, and pharmacology.

PET Challenges

PET images used in research and medicine require high resolution, low noise, and a high degree of contrast. Implementation of PET systems poses several challenges which add to noise contributions in resulting images. These challenges arise from the nature of positron emission, as well as the nature of and limitations to conventional PET detectors.

Positron emission is the process by which unstable radioisotopes with an excess amount of protons decay by ejecting a positron, the anti-particle to the electron, out of the atom with a definite energy. The positron scatters in the surrounding matter, losing energy through Coulomb interactions before annihilation with a nearby electron. The distance of travel of the positron is dependent on the energy with which the positron was emitted. In the case of 18F, positrons can travel more than 3 mm before annihilation, and generally travel approximately 1 mm. This travel within matter is generally referred to as positron range.

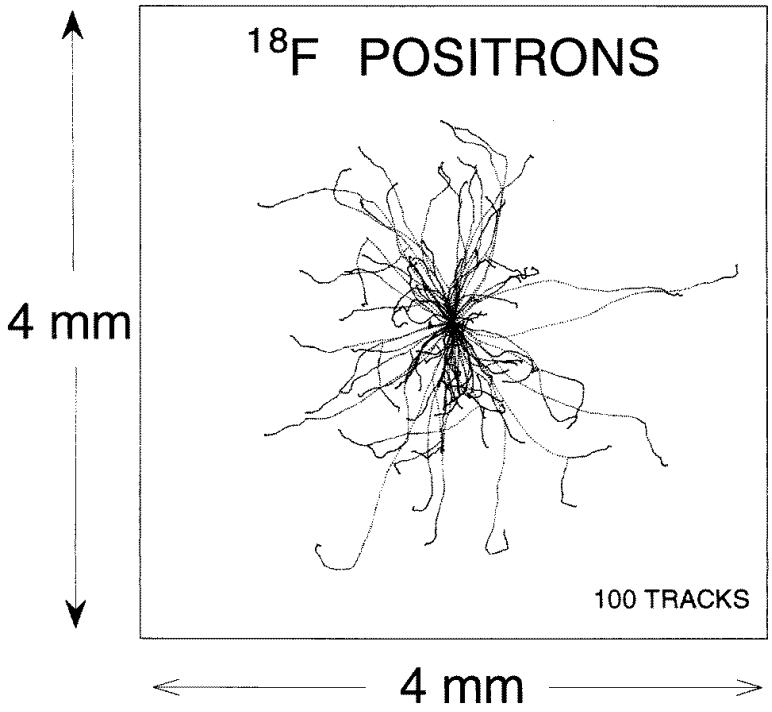

Figure 1.1.1: Representation of positron range in water from the radioactive decay of 18F (2). Positron tracks were simulated with Monte-Carlo code. The positron range is one of the causes of blurring contributions to reconstructed images in PET systems.

Since emitted positrons and electrons in orbit both have a certain amount of momentum, conservation of momentum upon annihilation gives small variations in the colinearity of the emitted photons (FWHM 0.5^{o}).

Positron range and acolinearity are intrinsic physical limitations of PET giving maximum requirements on spatial resolution of reconstructed images.

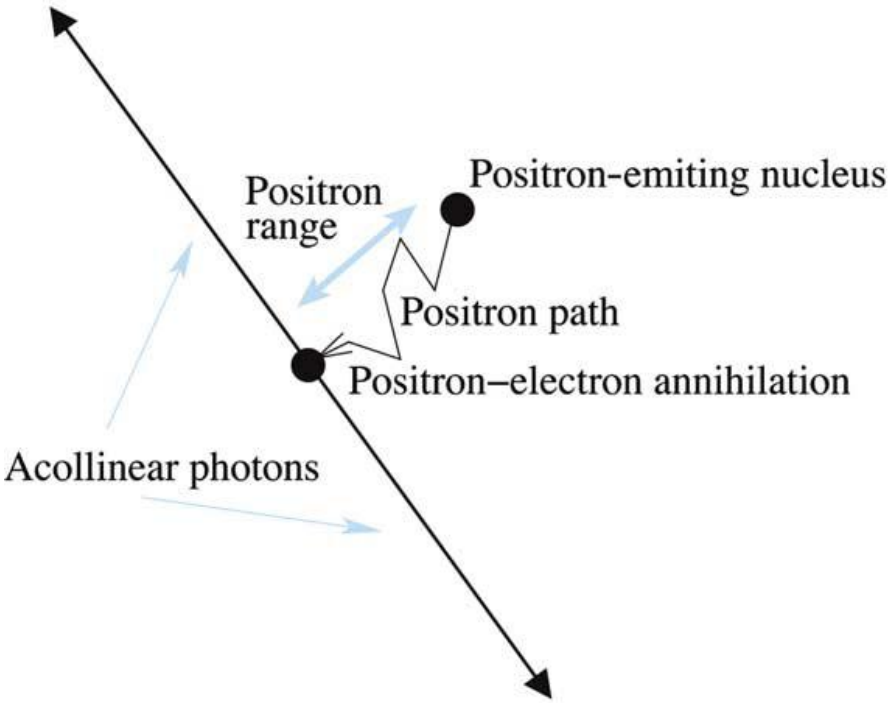

Figure 1.1.1: Representation of Acolinearity in annihilation photons due to the non-zero energy and momentum of the positron and annihilation electron. Acolinearity is another factor for blurring contributions in PET systems. Image taken from (3).

The combination of positron range and acolinearity of annihilation give rise to deviations between the calculated LOR and the actual location of the emitted positron, which manifests itself as increased blurring in the reconstructed image.

Further limitations also arise from the nature of the PET detector, due to the finite detector element size, energy resolution, and limitations in timing resolution, which contribute to limitations in reconstructed images such as limitations in spatial resolution, signal-to-noise ratio, and count rate. The main contributions to noise in the resulting image are due to three types of mis-identified LORs: random events, scatter events, and parallax error.

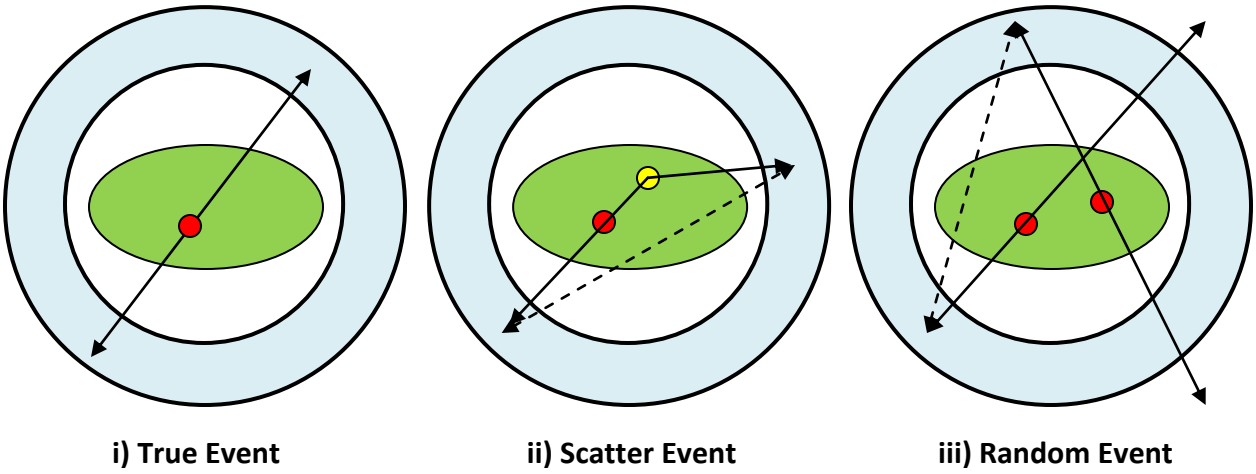

Figure 2: Schematic representing two of the main factors contributing to noise: random and scatter events. The mis-reconstructed LORs from these types of events contribute to noise in reconstructed PET images. Modern PET detectors employ a number of methods to try to reduce the contributions of random and scatter events, which is one of the main goals of the LXePET system.

Random events arise when photons from two separate annihilations are detected coincidentally creating a LOR where no source was present. As the activity of the source radioisotope is increased, the probability of detecting separate annihilations coincidentally is increased quadratically. This poses a significant problem for short-lived radioisotopes used in PET, since a high activity source must be used in order to obtain the amount of LORs necessary to generate statistically significant images.

Radioisotope	Half Life
11-C	20.38 minutes
13-N	9.97 minutes
15-O	2.04 minutes
18-F	1.83 hours

Table 1: Commonly used isotopes in PET show a large range in half life, however most are quite short (less than 2 hours). This emphasizes the need for detection systems with high count rate capabilities that can be used with high-activity sources.

Several methods have been employed to attempt to reduce the contributions of random events to the overall noise both in detector construction and statistical subtraction. An increase in the timing resolution in PET detectors, such as with time-of-flight PET, (4) gives an increased ability to resolve random coincidences, but this is limited by the time of flight of annihilation photons, which depends in turn on the detector size and size of the patient being imaged. Statistical subtraction methods such as delayed sampling (5), and calculation of random rates based on individual detector element event rates (6) have also been employed in certain detector configurations to reduce random contributions by approximately 20% (5). Random noise contributions are also reduced in image reconstruction by eliminating the LORs that did not pass through the subject, but a complete elimination is not easily performed. Typical PET systems have random fractions in the range of 35-40% (7).

Scatter events arise from photons that scatter within the subject through the Compton or Rayleigh process before being detected, generating mis-identified LOR. Conventional PET systems typically have scatter fractions in the range of 30-40% when operated in 3-D mode, and 15-20% when images are taken as 2-D slices (8). Since most scatter events occur through the Compton process, there is a definite energy loss of the scattered photon. LORs arising from scattered photons are generally eliminated by having an energy cutoff window above the Compton edge, which is in turn limited by the energy resolution of the detector. Increasing the energy resolution of the PET detector will thus decrease the contribution of scatter events by eliminating photons with less than 511 keV that are used in the generation of LORs. Ideally,

one would eliminate all photons detected with less than 511 keV, however this is unrealistic in practice since the energy resolution achievable with modern PET systems (typically ~20% FWHM, modern high-resolution systems ~14% (9)) requires a wider energy window in order to not eliminate true coincidences and ensure good detection efficiency and overall detector sensitivity.

Parallax error arises from the fact that most conventional detectors employ scintillation elements of a finite size and depth. Interactions of gamma photons with these elements create thousands of optical photons through the scintillation process, which are then detected by optical photon detectors such as photomultiplier tubes (PMTs) or photodiodes. Scintillation is generally isotropic, therefore interactions within the detector elements have very little or no information as to the depth of the interaction (DOI). Detected photons are assigned a fixed location within the detector (usually near the center of the element) from which a LOR is generated. The difference in the actual interaction and the assigned location can create parallax error in the reconstructed LOR, which contributes to noise in the resulting image. Furthermore, there is a significant probability that the annihilation photon will not be photo-electrically absorbed, but instead will undergo a series of Compton scatter events within the detector elements. In order to identify the true path of the photon, it is necessary to identify the order of these interactions. Temporally distinguishing the order of interactions is unfeasible, since interactions occur within a short range and too small of separation in time. In the case of all interactions occurring within the same detector element, this is not necessary, since the detector will "see" the event as a single photoabsorption, however, many scatter events occur within adjacent detector elements. In this case, an energy weighted average of the interaction location among adjacent elements will result in parallax error in the reconstructed LOR, proportional to approximately half the distance between the centers of the adjacent elements. Generally, Compton events in two or more crystals are simply rejected, which limits the ability to construct PET systems with large amount of event acceptance, since a large number of events undergo Compton scatter within the detector.

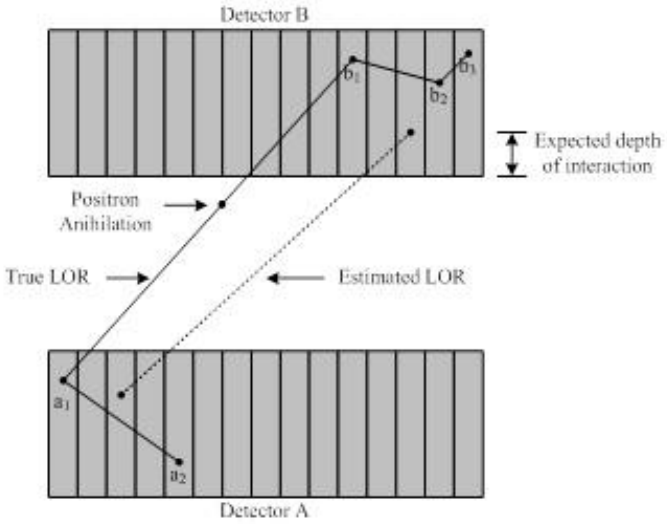

Figure 3: Representation of parallax error resulting from scatter within detector elements and depth of interaction miscalculations. Crystal scintillator based PET systems have limitations in their ability to identify the depth if interaction within elements, as well as in their ability to reconstruct simultaneous scatter events within detector elements. Image taken from (10).

Several methods have been employed to conventional PET detectors to reduce the noise contributions arising from detector limitations; however most are limited by the finite detector size and resolution in energy and time. Reduction of the detector size and improvements in energy and time resolution generally require increased construction and maintenance costs of the detector, and attempts to eliminate detector noise contributions with conventional detectors have been unsuccessful or prohibitively expensive. The liquid xenon PET (LXePET) project is an attempt to eliminate the detector contributions to noise, and reduce overall noise contributions to the essential physical limitations of positron range and non-colinearity.

Manufacturer	Philips		Siemens		GE Healthcare	
Characteristic	GEMINI TF Big Bore	GEMINI TF PET/CT	Biograph mCT	Biograph TruePoint	Discovery VCT	Discovery PET/CT 600
3-D Sensitivity (cps/kBq/cc)	7.2	7.2	9.5	7.6	9.1	9.1
Scatter Fraction (%)	31	30	<36	<36	36	38
Min. Transverse Resolution (mm)	4.7	4.7	4.4	4.2	5.0	5.1
Min. Axial Resolution	4.7	4.7	4.5	5.2	5.0	5.6

Table 2: Performance characteristics of conventional PET systems in clinical use. Data obtained from (8).

LXePET Project

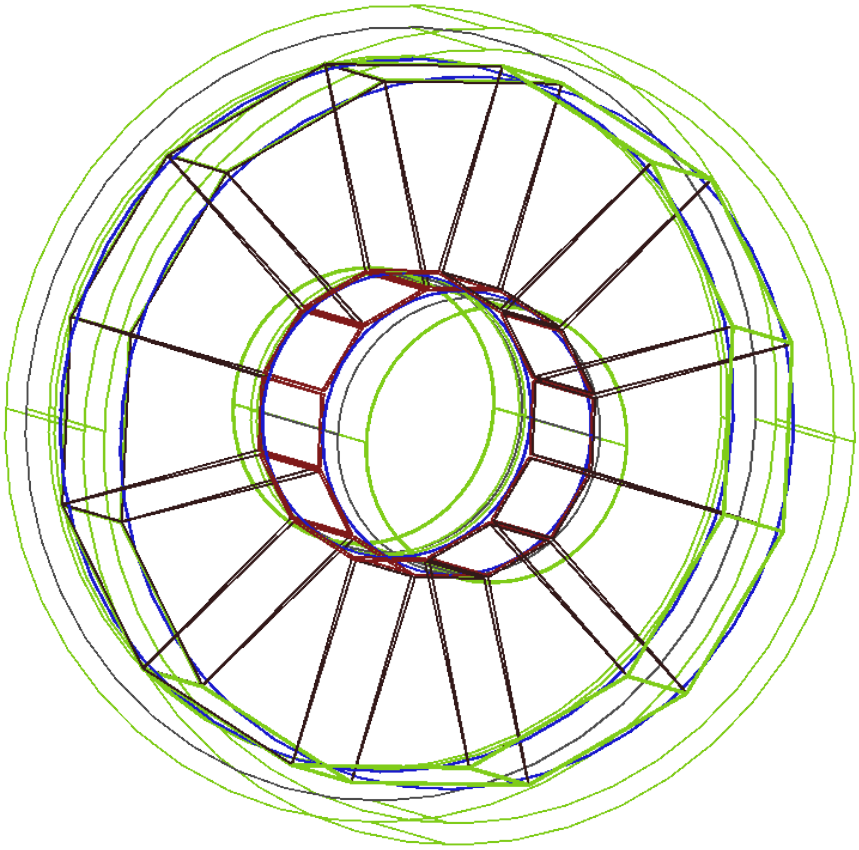

Figure 5: Wire frame representation of the main detector elements of the LXePET prototype. Conventional crystal scintillator blocks have been replaced with trapezoidal chambers filled with liquid xenon. The detection method is dual format wherein ionization charge and scintillation light measurements are combined to increase detector energy resolution.

Liquid xenon has been used in many high energy physics experiments as a detection medium (11) (12) (13), and has several properties that make it applicable for use in PET (14). The relatively high density (2.9 g/cm^3) allows for a high gamma photon interaction cross section, and the relatively high atomic number (54) allows for a good photo-electric cross section (approximately 22% of interactions at 511 keV are photoelectric), which is very suitable for PET

measurements. In addition, liquid xenon is a very good scintillation material, although in the UV at 178 nm, with a photon yield (W) of 14.6 eV per photon at zero electric field. Scintillation decay of LXe has two components: a slow decay of approximately 29 ns, and a fast decay of approximately 2 ns which lends itself towards good coincidence timing windows that are comparable to the best scintillation crystals. Furthermore, the ionization yield of 15.6 eV per ion pair created (about 64000 ions per MeV absorbed) allows for the collection of electrons by a drift chamber, where the electrons are drifted under a high electric field and collected at an anode. Liquid xenon is readily available at high quantities, and its use has been studied well in many experiments.

The LXePET prototype consists of twelve trapezoidal chambers filled with liquid xenon. They are housed in a cryostat containing liquid nitrogen in order to retain the liquid state of the xenon (See (15) for a detailed description). Interactions of high energy gamma photons with the xenon produce scintillation light as well as ionization charge in the form of a cloud of electrons. Scintillation light is collected by 48 large-area avalanche photodiodes (LAAPDs) arranged in arrays of 24 on opposing sides of the chamber. Ionization charge is collected by placing the chamber under a high electric field and drifting the electron cloud towards a segmented anode of 96 strips with 1.1 mm separation. Prior to the anode is a perpendicular array of 96 induction wires (see (16)). The three dimensional position of interaction of gamma photons within the liquid xenon is calculated in two ways: first using the scintillation light on the LAAPD arrays, and second using the ionization charge. Using scintillation light to quickly determine the rough position of interaction is essential to limit pile-up for the slow ionization signals which give the high (sub-mm) resolution measurements. Knowledge of the rough locality of the ionization allows for ignoring other events that occur within the detector during the drift time interval (approximately 60 μs). This is an important feature of the system.

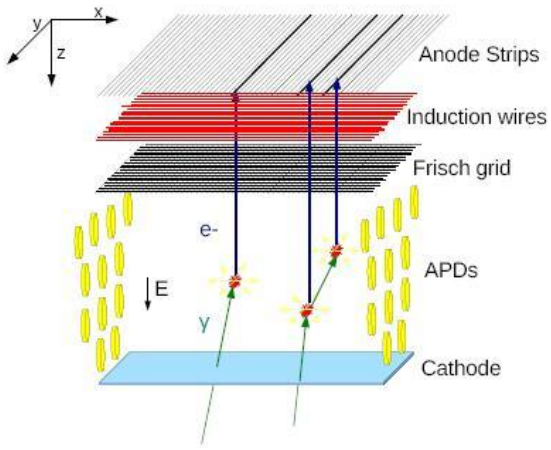

Figure 6: Representation of the detection method of the LXePET prototype. Scintillation light is detected by parallel arrays of LAAPD light detectors, and ionization charge is drifted under an applied electric field through an array of induction wires toward a segmented anode. Fully 3-dimensional positions of interactions are reconstructed with sub-millimeter precision. Figure taken from (15).

The calculation of position of interaction from the scintillation light is performed using neural network algorithms, which will be further discussed in this thesis. One dimension of the 3-dimensional position calculation from the ionization charge is performed by measuring the difference between the time of the scintillation trigger on the LAAPDs and the time the ions reach the anode. The other two are obtained by interpolating the signals from the segmented anode and induction wires, thus providing a fully 3-dimensional representation of the position of interaction for each ionization deposit within the chamber.

A small scale prototype liquid xenon detection chamber has been built and initial measurements have been performed (16). By combining measurements of scintillation light and ionization charge, it was found to be capable of energy resolution of 7.5% FWHM, with sub-millimeter resolution of interaction locations in 3 dimensions. Similar liquid xenon detectors have been shown to be capable of even better energy resolution (~4% FWHM) with the possibility of even higher resolution (~2.5% FWHM) (17). This is a significant advantage over conventional scintillation crystals used in PET both in terms of energy resolution (see Fig.8) and

the ability to identify the exact location of interaction within the detector. In addition, higher sensitivity can be achieved because of the ability to resolve multiple interaction points within the detector and the large active volume of detection.

Scintillator	BGO	LSO	NaI (Tl)	LXe
Density (g/cc)	7.1	7.4	3.67	3.1
Scintillation Yield (photons/keV)	6.4	32	40	68
Decay Time (ns)	300	40	230	2.2 / 27
Wavelength	480	420	420	178
Photo-electric Fraction	42%	33%	17% (NaI)	22%

Table 3: Comparison of some of the detection characteristics of liquid xenon to that of conventional ceramic crystals used in PET systems. The physical properties of liquid xenon make it a suitable medium for gamma photon detection.

In addition to the physical detection properties, liquid xenon has the ability to distinguish multiple Compton scatter events from the same annihilation photon within the same detector element, which allows for increased scatter reduction techniques which will be further discussed in later sections. This relies on the ability to correctly distinguish and identify the order of interactions within the detector.

Compton scatter occurs when a high energy photon interacts with an electron in one of the outermost energy levels of an atom (i.e. a 'free' electron). The collision transfers energy to the electron which is ejected from the atom along with a photon (the 'scattered' photon) of energy equal to the initial photon energy minus the sum of the binding energy of the electron and the energy imparted to the electron. The kinematics and interaction cross section of Compton

collisions are well known and can be used to estimate the order of interactions of multiple Compton scatter events. Since only approximately 22% of interactions of 511 keV photons are photo-absorptions, Compton scatter events represent a significant portion of detections. Knowledge of the order of Compton events within the detector eliminates blurring due to parallax error as discussed previously. Since Compton reconstruction also gives knowledge of the direction of the incoming photon, additional rejection of random coincidences is possible. Furthermore, since the order of interactions is given as a probability distribution, weighting schemes can be devised which can reduce scatter contributions significantly, as will also be discussed.

Chapter 2: Monte Carlo Simulations

Monte Carlo simulations of the LXePET prototype as well as for single sectors within the prototype were performed using GEANT4 (18) and analyzed with the ROOT (19) software analysis package. GEANT4 is a well established toolkit for the simulation of the interaction of particles with matter developed for use in high energy and nuclear physics. Its application to nuclear medicine is straightforward since interactions with high energy gamma particles are studied. ROOT is a data analysis framework which consists of an object oriented program and library, which was mainly used for histogramming, graphing, and curve fitting of data. Neural network algorithms including the TMultiLayerPerceptron class used in later sections were taken from ROOT (20).

Detector Configuration

The LXePET prototype was simulated in full as well as in a single sector configuration. The full prototype configuration was used to simulate the detector response for annihilation events within various phantoms. The single sector configuration was used to simulate the LAAPD response of single scintillation events within the sector.

Single Sector

The single sector configuration consists of a trapezoidal chamber composed of copper anode and cathode plates of 50 μm thickness along with a field cage and APD support plates. The LAAPDs are covered by a trapezoidal quartz plate of 1.5 mm thickness. The specifications of the simulated construction are outlined in Table 4.

Detector Specifications for the LXePET single sector used in Simulations	
Axial Length	96 mm
Anode Width	104 mm
Cathode Width	40.5 mm
Radial Depth	114 mm
LAAPD Radii	8 mm, 5 mm, 2.5 mm
LXe Refractive Index	1.57
LXe Absorption Length	100 cm
LXe Rayleigh Scatter Length	35 cm

Table 4: Specifications of the single-sector prototype used in Monte-Carlo simulations. Parameters that were not relevant to the simulation such as the segmentation of the anode, induction wires, and Frisch grid were not included in this simulation.

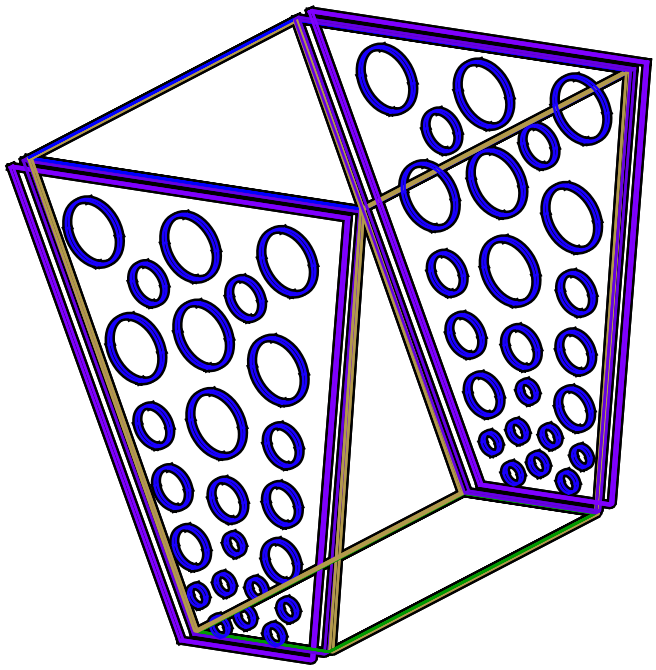

Figure 7: Wire frame representation of the single sector prototype used in the Monte-Carlo simulations. Optical photons were generated within the sector and tracked until absorption. Optical photons absorbed within the LAAPD surfaces were tabulated into ROOT histograms.

In this configuration, simulated scintillation events were generated at locations throughout the entire active volume of liquid xenon. Specifically, 10220 optical photons of energy 7.0 eV were generated with an isotropic spherical distribution at locations throughout the active volume in a 2x2x2 mm grid. The path and interactions of the optical photons were tracked throughout the chamber. The number of optical photons that were absorbed on each of the LAAPD surfaces (considering probability of reflection) was tabulated for each of the locations simulated. This process was repeated with optically reflective surfaces added to the inner walls of the chamber resembling that which is practically achievable in the prototype. In this case, polished reflective surfaces with an 80% probability of reflection were added to the cathode. The instrumental response of the LAAPDs was not applied to the simulation, but was added to the data during analysis.

Full LXePET Prototype

The full LXePET prototype configuration consists of twelve trapezoidal sectors arranged in a ring geometry, immersed in a vessel filled with liquid xenon. The liquid xenon vessel is housed in a stainless steel vacuum cryostat of 1 mm thickness. The sectors are composed of a ceramic cathode plate, steel plates to house the LAAPDs, and a 1.5 mm stainless steel plate backing the anode. For the purpose of interactions with 511 keV gamma particles, the polycarbonate field cage is sufficiently taken into consideration with the stainless steel LAAPD plate. The specifications of the simulated construction are outlined in Fig.10.

Detector Specifications for the full ring LXePET prototype used in simulations	
Axial Length	100 mm
Sector Height	112 mm
Cathode Length	32 mm
Anode Length	92 mm
Inner Air Tube Radius	49.8 mm
Vacuum Cryostat Inner Radius	59.8 mm
Vacuum Cryostat Outer Radius	114.3 mm
Xenon Chamber Outer Radius	225.0 mm

Table 5: Specifications for the physical construction of the full ring LXePET prototype used in Monte-Carlo simulations. Parameters and components not relevant to the simulation such as segmentation on the anode, induction wires, xenon and nitrogen circulation components, and Frisch grid were not included in this simulation.

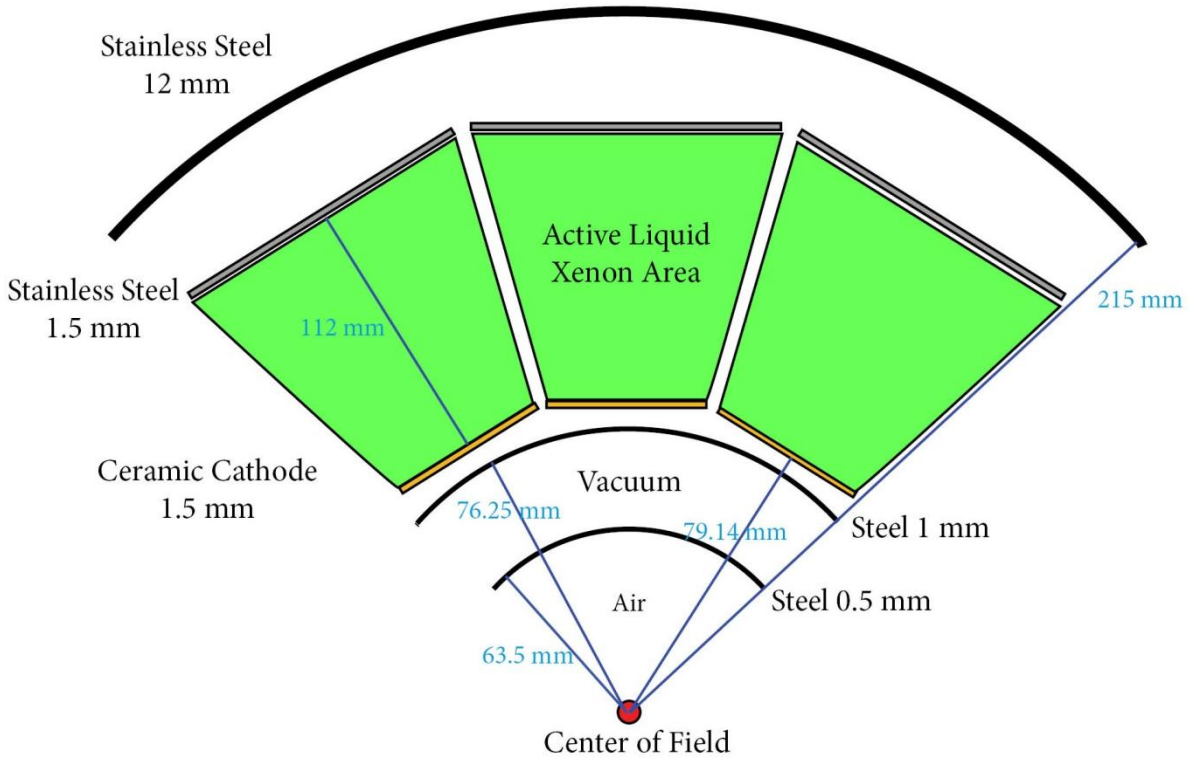

Figure 8: Cross-sectional representation of the construction of the full-ring LXePET prototype as used in Monte-Carlo simulations. Distances represent the radial distance from the center of the field to the inner edge of the specified component. Distances and sizes are not to scale.

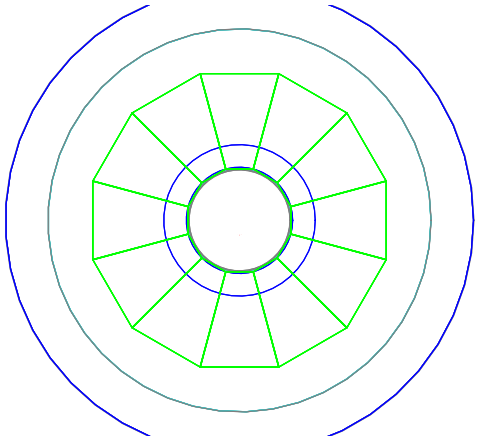

Figure 9: Cross-section highlighting the active liquid xenon area within the LXePET detector configuration.

The full prototype simulation was carried out by generating a positron emitting source (18F) of a specific size and distribution within phantoms described by NEMA (21) standards. In this case, we used both the Rat-Like NEMA phantom and the Mouse-Like NEMA phantom, with embedded 18F sources. These phantoms consist of polyethylene cylinders with embedded cylindrical water filled sources arranged coaxially with the phantom cylinder with a radial offset. The specifications of the NEMA standard phantoms are described in Fig.14.

Specifications of NEMA standard phantoms used in Simulations

	Rat-Like NEMA Phantom	Mouse-Like NEMA Phantom
Cylinder Diameter	50 mm	25 mm
Cylinder Length	150 mm	70 mm
Source Diameter	3.2 mm	3.2 mm
Source Length	70 mm	70 mm
Radial Offset	17.5 mm	10 mm

Table 6: Specifications of the physical dimensions of the NEMA standard phantoms used in the full ring LXePET prototype simulations. Both phantoms were composed of polyethylene with the source distributed uniformly in a water medium.

The energy of the emitted positron is given by the specific decay probability and energy distribution of 18F. The momentum and position of the positron upon annihilation was recorded, and a method for simulating the non-colinearity due to the non-zero momentum of the positron was implemented. The momentum and polarization of each of the annihilation photons was recorded. Interactions of the annihilation photons were recorded and categorized according to the medium with which they interacted. For each interaction within the active liquid xenon volume, the position and energy deposited were recorded. The detector response to the interactions within the liquid xenon was applied at a later stage, and not during the initial Monte-Carlo Simulation.

Chapter 3: Single Sector Analysis – Reconstruction With Neural Networks

The GEANT4 simulation of the single sector generated a database of scintillation photons reaching each LAAPD for locations throughout the entire active area of the sector in the form of ROOT histograms. Detector response parameters were then applied to the histogrammed data using ROOT analysis software. The resulting data was then used as a kernel for training a neural network based on the ROOT TMultiLayerPerceptron class. The performance of the neural network in correctly reconstructing scintillation positions was then analyzed for reflective and non-reflective cases with various noise levels applied to the detector response.

Description of Neural Networks

Neural networks (NNs) are computational models that mimic the response of biological neural networks. In biology, information is transferred and processed by sending electrical signals through an interconnected group of neuron cells. These cells have several input connections (synapses) to surrounding cells through which a signal is passed to a central axon as the output. The learning process of neural networks was discovered in 1949 by Hebb (22) in which the signals received by a synapse and sent to the central axon can alter the synaptic connection, thus either inhibiting of facilitating communication by that synapse. In the case of computational or artificial neural networks, the network adapts its structure based on learning inputs. Neural networks are used in computational models to model complex relationships and identify patterns in data.

In our case, the number of scintillation photons reaching the LAAPDs is used to train the network to be able to identify patterns in the signal resulting from scintillation at a specific location within the chamber. The network consists of three parts, the input layer, the hidden layer(s), and the output layer, which are connected by weighting matrices. The input layer consists of the signal of each individual LAAPD for a specific location within the chamber, which is given by applying individual detector response to the number of photons reaching that APD. In this case, we used a hidden layer composed of 160 ‘neurons’, which form the intermediate stage wherein the structure and response of the NN is adapted. The output layer is simply the location of the scintillation as predicted by the NN. The NN employs an iterative optimization method known as the Broyden-Fletcher-Goldfarb-Shanno (BFGS) method, which approximates

Newton's method (23), and the learning was applied for 200 iterations which allowed for sufficient convergence.

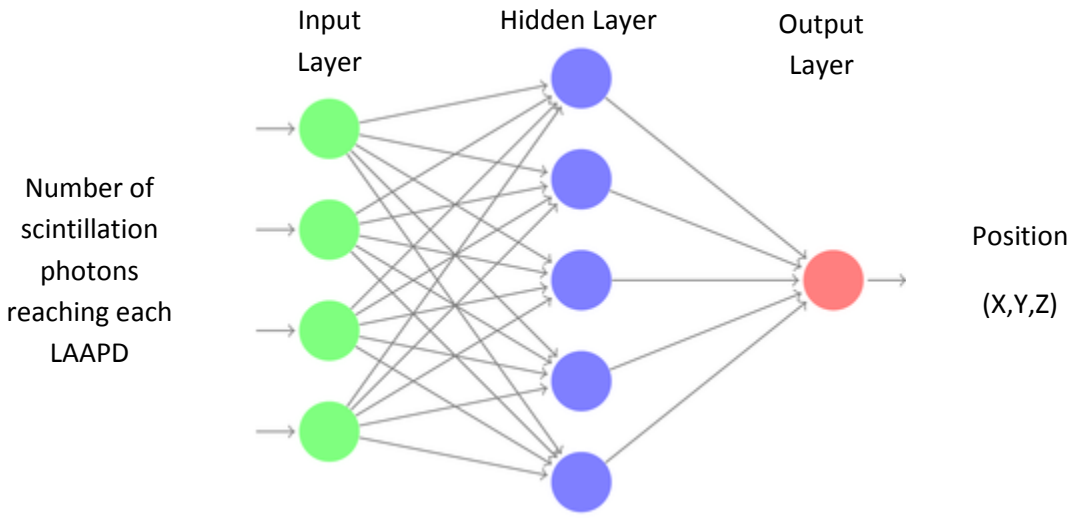

Figure 3: Schematic representation of the structure of the Neural Network used in this study. The network consists of 3 layers: input, hidden, and output, which are separated by weight matrices. The number of scintillation photons reaching each APD was used to calculate the 3-dimensional position of scintillation.

Implementation of NN Algorithms

The LXePET prototype requires a robust method for distinguishing interaction locations in the first stage of the event selection process. The fast scintillation response allows for high count rates and timing window resolution, however, the ability to separate events from unique annihilation photons is necessary in order to provide correct interaction locations. This is especially relevant in time dependent scans where a relatively high activity source is used and a time lapse of activity distributions throughout the patient is required. The NN algorithm has been proposed as a viable method for the first stage event selection. In this case, the number of scintillation photons reaching each LAAPD for possible scintillation positions within the single sector on a 2x2x2 mm grid spacing (N_i^p) was used as the input layer to train the neural network. Since the NN performance is related to the amount of training data available, a random scintillation location was generated in the chamber, and the resulting optical photon signal

from that location was retrieved from the database. Electronics noise was then applied to the signal on each LAAPD to represent the actual signal which the prototype would receive (see next paragraph), and the resulting data was used as the input layer for the NN algorithm.

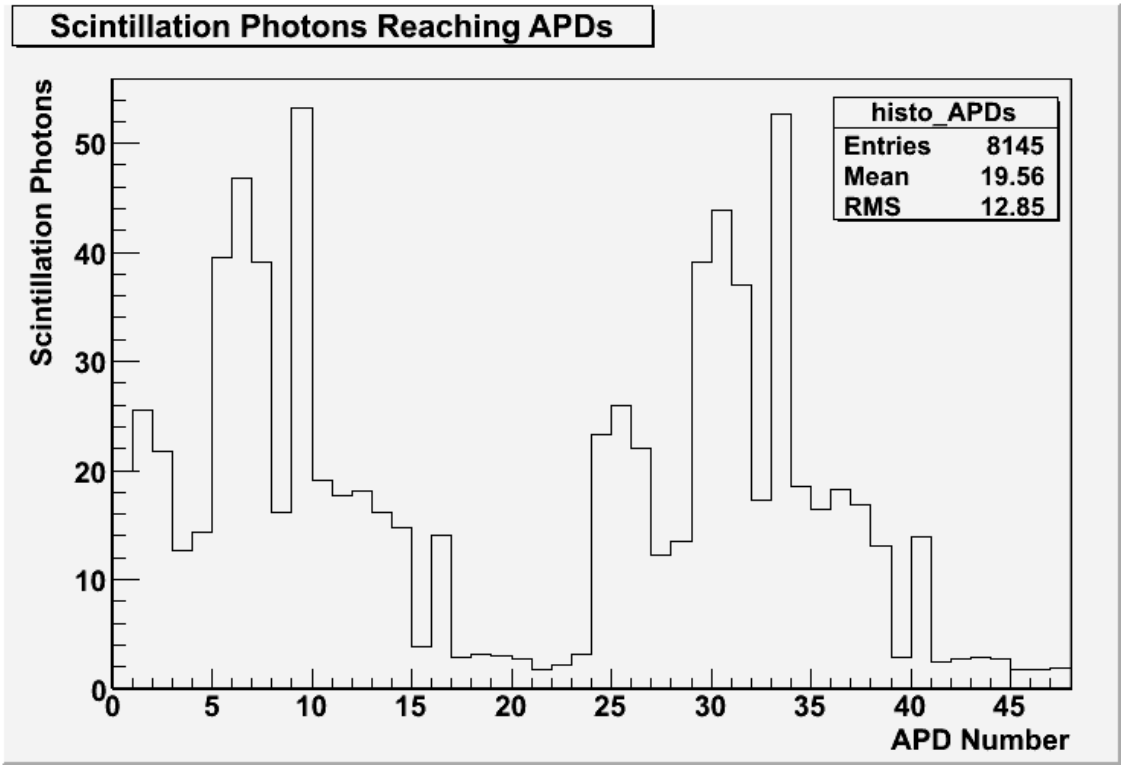

Figure 4: Sample histogram of the number of scintillation photons absorbed at APD surfaces for a scintillation location in the center of the sector. Simulations were performed 100 times for each location and averaged to minimize statistical fluctuations.

This was repeated for 200,000 random locations in the chamber. This number was chosen as a suitable trade-off between NN performance and computation time for the training. This process was repeated for the case of reflective surfaces within the chamber. The resulting NN was then used to identify locations from randomly generated signals within the chamber. In this case, in order to fully approximate the signal processed by the detector, the number of photons reaching the LAAPD surface (N_i^p) which originated from the simulated location r_s was converted to the expected signal (N_i^e) resulting from the stimulus of the optical photons on the APDs (in units of scintillation photons). The number of photo-electrons N_i^{pe} resulting from the

optical stimulus is generated from a Poisson distribution centered at $N_i^p * QE$, where QE is the quantum efficiency of the APDs (set to 0.8, which is below maximum QE of LAAPDs in liquid xenon at 178 nm (24)). Statistical fluctuations in N_i^e were approximated by a Gaussian distribution parameterized by:

$$\sigma_G = \sqrt{\left(\frac{Noise}{Gain}\right)^2 + (ENF - 1)N_i^{pe}}$$

Where $Noise$ is the specific APD noise factor based on the size of the LAAPD (in electrons), and ENF is the excess noise factor ($ENF = 2.5$). The resulting expected signal (N_i^e) was generated for random locations throughout the chamber. The trained NN was used to calculate the expected scintillation position r_p resulting from a detected signal given by N_i^e. The difference between the simulated position and the calculated position was used to quantify the ability of the NN to distinguish events within the sector.

Position Reconstruction Results

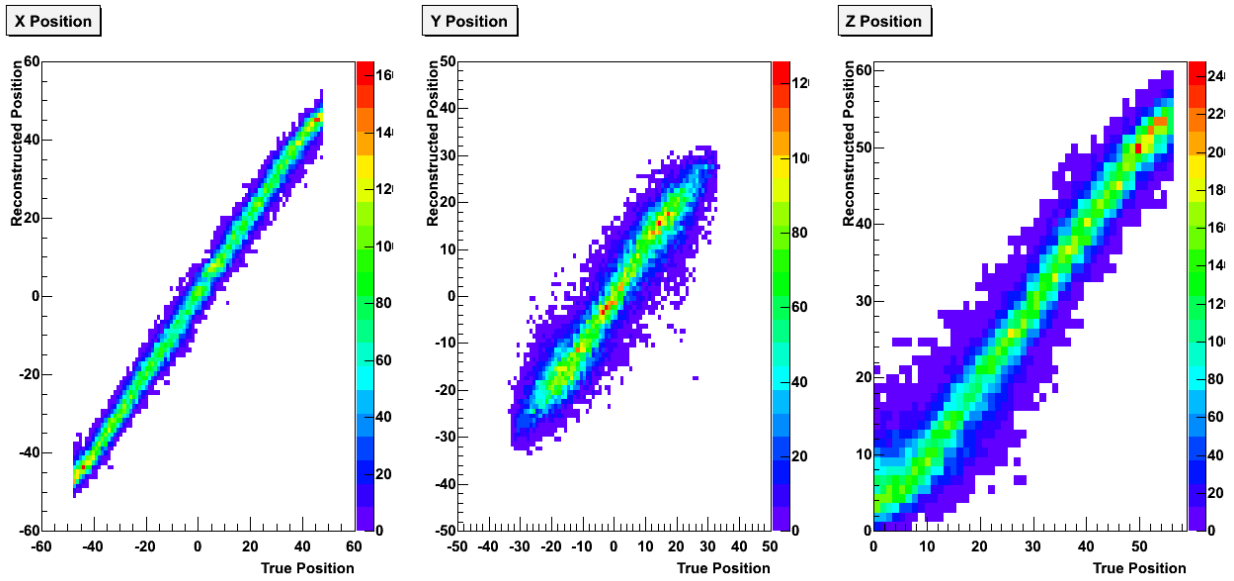

Figure 5: Position of interaction reconstructed by the NN algorithm versus actual position in X (axial), Y (tangential), and Z (radial) directions.

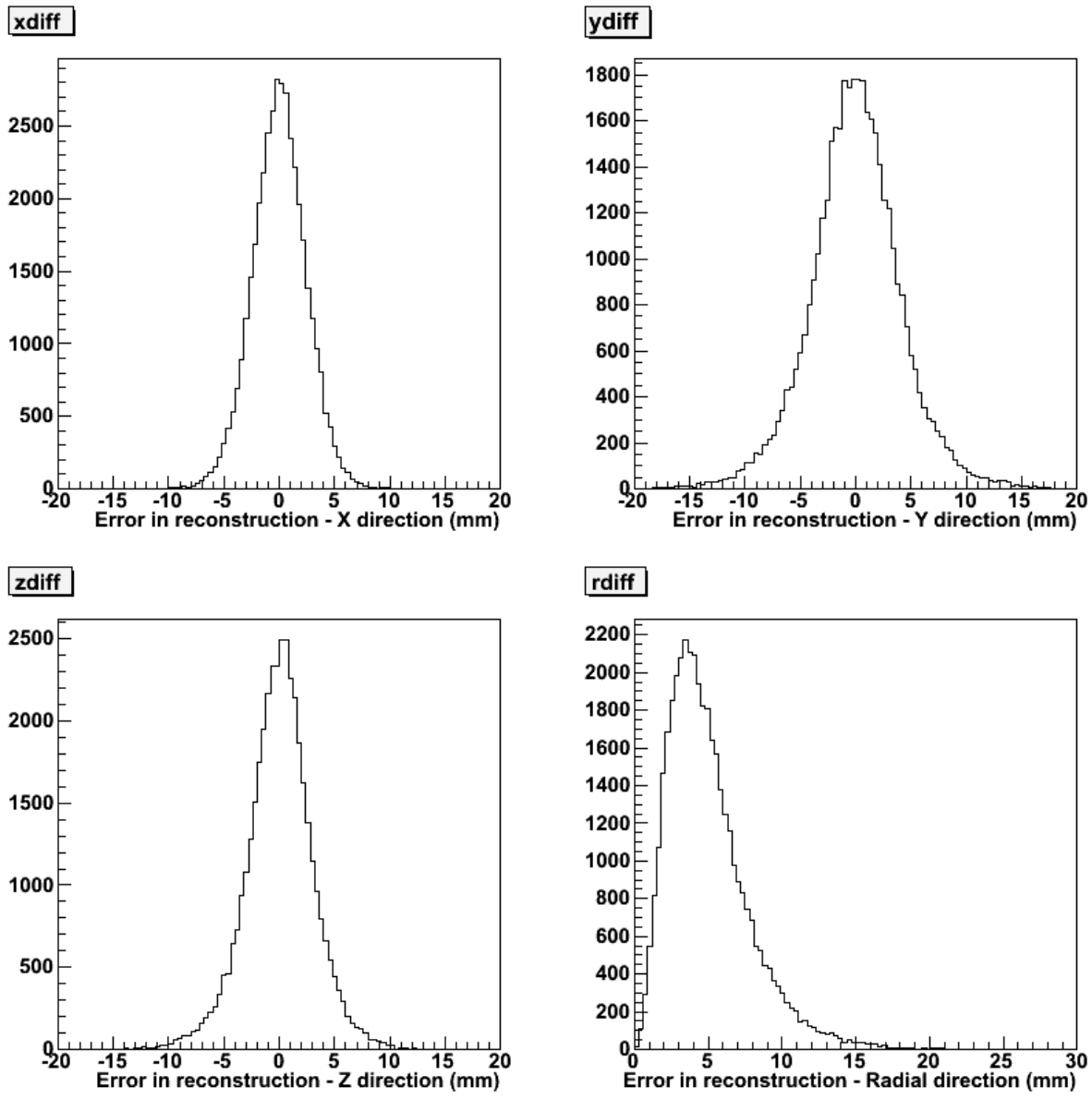

Figure 6: Example of the error in reconstruction of scintillation position in the X, Y, Z, and radial directions for a case of reflective surfaces in the chamber. In this case, electronics noise of 500e- was added to the data.

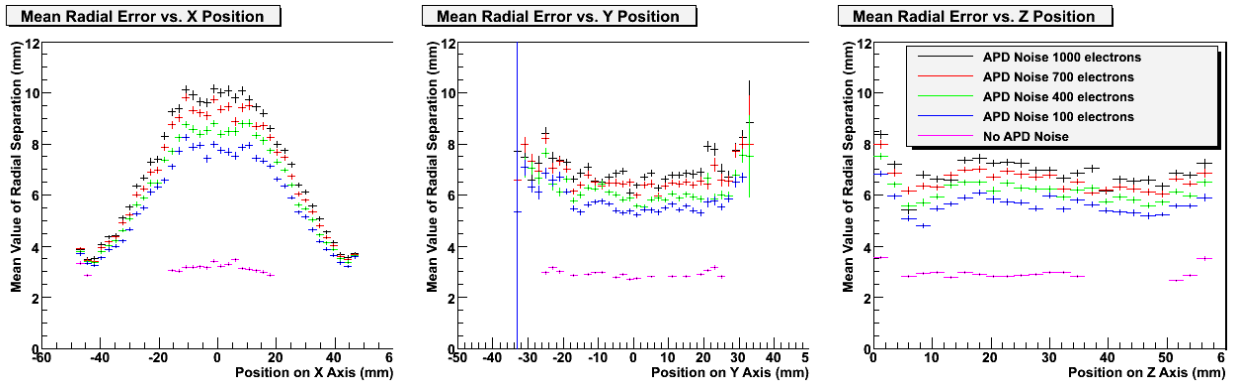

Figure 7: Mean reconstruction error (radially from the actual point to the reconstructed point) as a function of position on X, Y and Z axes, plotted for various noise levels on the APDs with reflective surfaces added to the chamber.

Noise Level	Reflectivity			No Reflectivity		
	FWHM – X (mm)	FWHM – Y (mm)	FWHM – Z (mm)	FWHM – X (mm)	FWHM – Y (mm)	FWHM – Z (mm)
1000 e-	7.37±0.04	12.04±0.07	9.65±0.05	6.96±0.04	11.02±0.06	8.85±0.05
700 e-	6.99±0.03	11.49±0.07	9.11±0.05	6.58±0.03	10.46±0.06	8.22±0.04
400 e-	6.45±0.03	10.97±0.06	8.41±0.04	6.07±0.03	9.85±0.05	7.69±0.04
100 e-	5.86±0.03	10.29±0.05	7.65±0.04	5.31±0.02	9.08±0.04	6.82±0.03
No Noise	3.74±0.02	4.87±0.03	4.33±0.02	3.42±0.01	4.45±0.02	3.92±0.02

Table 7: Reconstruction results of the NN algorithm for reflective and non-reflective surfaces on the inner walls and various noise levels on the LAAPDs.

Results of the NN algorithm in reconstructing the scintillation positions show that for both cases of non-reflectivity and reflectivity, reconstruction in the Y direction (tangential) is the least accurate. This is most likely due to the location and orientation of the LAAPDs, since variations in position along the Y axis have less effect on the signal reaching the APDs than variations in the X (axial) and Z (radial) directions. This is confirmed by the fact that along the X axis, the least accurate reconstruction results are near the center (X=0 mm), while near the APD planes (X=±55 mm) the reconstruction is the most accurate. Increases in electronics noise caused increases in the FWHM of the reconstructed points in X, Y, and Z as expected for both cases of reflection and non-reflection. The most notable results are the fact that adding reflective

surfaces did not have a strong effect on the ability of the NN algorithm to reconstruct scintillation positions, the reconstructed errors were comparable. This is important because the addition of reflective surfaces serves to increase the total amount of scintillation photons reaching the APDs which increase the signal-to-noise ratio of the APDs and the energy resolution. Further studies and the addition of other reflective surfaces can serve to quantify this improvement.

Chapter 4: Full LXePET Prototype Analysis

In order to gain a better understanding of the capabilities of a micro-PET system based on liquid xenon, it was necessary to simulate the entire LXePET prototype including reconstruction of a final image. Monte-Carlo simulations of the full LXePET ring prototype were performed for both the Rat-like and Mouse-like NEMA standard phantoms. Locations of interactions of annihilation gamma photons within the active liquid xenon volume were categorized into a ROOT class created for the simulation. The class contains information on location and energy deposition of the interaction, statistical information about the number or sectors a specific photon interacted with and the types of interactions, as well as the annihilation location and acolinearity of the photons. Parameterized detector response was applied to interactions on a point by point basis, which approximated the system capabilities including energy and spatial resolution of the detector. Sinograms as well as list-mode LOR information were calculated from the resulting data.

Detector Response

The LXePET system capabilities have been analyzed previously with a small scale prototype (16). From this, the system response can be parameterized and applied to simulated interaction locations within the active detector area. For annihilation events *i* which produced photons that interacted within the active detector area, the simulated photon interaction position r_i^S and energy deposited E_i^S were recorded. Since the detector is only able to resolve events with approximately 1mm FWHM spatial resolution, multiple events that occurred within 1 mm were merged into a single event, with the energy deposited summed and the location given as an energy weighted average of the combined interaction locations. Blurring was applied to the interaction locations in the form of a Gaussian distribution with a width of 1 mm. The detector response applied to interactions as described by (15) proceeded as follows.

From the energy deposited, the number of scintillation photons S_i^S and ionization electrons I_i^S produced in the interaction were calculated by

$$S_i^S = \frac{(SF + Fr^*) * E_i^S}{15.6eV}$$

$$I_i^S = \frac{(1 - Fr^*) * E_i^S}{15.6eV}$$

where Fr^* is the electron-ion recombination fraction modified to include fluctuations due to the light-charge anti-correlation fluctuation of liquid xenon (17), and SF=0.2 is the ratio of the number of scintillation photons and ion pairs produced at the electric field strength used in the prototype (17). The light-charge fluctuation was taken from a Gaussian distribution with a mean of Fr=0.24 and standard deviation of 0.032 (16). Electronics noise was added to the ionization electrons I_i^S in the form of Gaussian blurring with a sigma of 600 electrons. A detection threshold of 1800 electrons was applied such that individual interactions with less than the required threshold were discarded. Thus, the total number of electrons detected I_t^D by the prototype was given as the sum of individual interactions (I_i^S) modified to include electronics noise and the detection threshold. The noise on the LAAPDs was given by a Gaussian distribution with a sigma given by

$$\sigma_{APD_j} = \sqrt{\left(\frac{ENC}{G}\right)^2 + (F-1) * P_i^{APD_j}}$$

where the number of photoelectrons generated by the scintillation light of the interaction on each APD ($P_i^{APD_j}$) is given by the Poisson function of the quantum efficiency of the APD (0.8) multiplied by the number of scintillation photons reaching the APD ($S_i^{APD_j}$). ENC is the equivalent electronics noise in terms of charge (1000 electrons), G is the gain (G=500), and F is the excess noise factor (F=2.5). In this case, the number of scintillation photons reaching the APD ($S_i^{APD_j}$) is calculated from the solid angle of the APD with respect to the scintillation position. No reflective surfaces are assumed in this case. Thus, the total number of scintillation photons detected S_t^D by the prototype was given as the sum of the individual interactions and corrected for the combined solid angle of the APDs

$$S_t^D = \frac{\sum_{j=1}^{J} P_t^{APD_j}}{\varphi\left(r_{cog}^S\right) * G}$$

where $\varphi\left(r_{cog}^S\right)$ is the fraction of the solid angle as seen by the combined APDs from the center of gravity of the interactions, and J is the total number of APDs (48). The energy deposited as detected by the prototype (E_i^D) was calculated from the combined signals from scintillation light (S_t^D) and ionization charge (I_t^D) as described in (25).

For this simulation, events within an energy window of 450-600 keV were selected as true, non-scattered events. This includes both single interaction photo-electric events as well as multiple Compton scatters followed by a photo-absorption, as long as the total energy deposited was within the energy window. The interaction locations and energies from the simulated data (true locations) along with the interaction locations and energies with the detector response applied (detected locations) were tabulated in the form of ROOT data trees. From the interaction points, list mode LOR files as well as sinogram files were created. The list mode LOR files contained the 3-dimensional interaction locations for events in which both annihilation photons deposited energy within the required window within the active detector area, and the

sinogram files contained the r and θ values for the LORs data with oblique slices combined into 2-D projections using the Single Slice ReBinning (SSRB) method (26) with 1 cm thickness of slices. For both the sinogram and the list mode files it is necessary to identify the first interaction points in order to be able to correctly identify the LOR. Since events with multiple interaction points within the detector involve single or multiple Compton scatters followed by a photo-absorption, a method of distinguishing interaction sequences must be employed. In this study, a method known as Compton Kinematics Discrimination (27) was used which statistically determines interaction order based on minimizing chi-squared values, which will be discussed in the next section.

Compton Discrimination

The method for discriminating interaction sequences for multiple interactions within the same detector was devised for astronomical observations with gamma ray telescopes (28). This method was implemented in the much the same way, however, the fact that in PET systems there exist two gamma photons absorbed simultaneously, the incoming trajectories can be ascertained to a good degree by the knowledge of the interaction locations on both sides of the detector simultaneously. However, absolute knowledge of the order of interactions is not possible due to insufficiencies in energy and position resolution, and the identification of first interaction points is given by a probability. Knowing the probability of an interaction being correct provides a basis for a method of reducing noise contributions from scatter which will be discussed in the next section.

In any annihilation event that is accepted as a LOR event (i.e., the energy deposited is within the 450-600 keV energy window), there are multiple scenarios in which the photons can be detected. For instance, both photons can be photo-absorbed (which we will refer to as a 1-1 event), which leaves no ambiguity in the order of interactions, and the LOR is simply the line connecting the two interaction points. However, it is more likely that the 511 keV photons will undergo Compton scatter within liquid xenon (LXe has only a 22% probability of photo-absorption at 511 keV), therefore there are a significant portion of events wherein at least one of the photons will undergo Compton scatter (i.e. 1-2, 1-3, 2-2 etc.). The basic premise of the Compton Kinematics Discrimination (CKD) algorithm is to calculate the probability of each

possible order of interactions based on chi-squared, and assign the correct first interaction point to the point with the least chi-squared value.

Compton scatter occurs when a photon interacts with an electron in one of the outermost energy levels of an atom (a 'free' electron). The 'collision' transfers energy to the electron and releases a 'scattered' photon with an energy equal to the incoming photon energy minus both the energy transferred to the electron and the binding energy of the electron (negligible in this case). Compton interactions have been well studied and interaction probabilities and kinematics can be readily calculated. The basis of the Compton interactions is given by the Klein-Nishina (29) formula which gives the differential cross-section $\frac{\partial\sigma}{\partial\Omega}$ of photon interactions as

$$\frac{\partial\sigma}{\partial\Omega} = \frac{1}{2}\left(\frac{\alpha\hbar}{m_e c}\right)^2 \{ P(E,\theta)^3 - P(E,\theta)^2 + P(E,\theta) + P(E,\theta)^2 \cos(\theta)\}$$

where $P(E,\theta)$ is the ratio of photon energy before and after collision given by

$$P(E,\theta) = \left[1 + \frac{E}{m_e c^2}(1 - \cos\ \theta)\right]^{-1}$$

For each multiple scatter event with *N* interaction locations there are *N-1* Compton scatters followed by a photo-absorption. For each interaction sequence, there are two possible ways to calculate the scattering angle: geometrically and with Compton kinematics (signified by subscripts G and E respectively). For the i^{th} interaction, the expected scattering angle $\theta_{E,i}$ from Compton kinematics for a photon with energy E_i is given by

$$cos(\theta_{E,i}) = 1 + \frac{E_e}{E_i} - \frac{E_e}{E_{i+1}}$$

where E_e is the rest mass energy of the electron ($E_e = m_e c^2 = 511keV$). Geometrically, we can calculate the scattering angle $\theta_{G,i}$ simply based on the location of the interactions as

$$cos(\theta_{G,i}) = \frac{\vec{r_i} \cdot \overrightarrow{r_{i+1}}}{|\vec{r_i}||\overrightarrow{r_{i+1}}|}$$

The probability that a given interaction sequence is correct is determined by a weighted chi-squared statistic based on the difference between scattering angles calculated in the two ways

$$\chi^2 = \sum_{i=2}^{N-1} \frac{\left(cos(\theta_{E,i}) - cos(\theta_{G,i})\right)^2}{\delta cos(\theta_{E,i})^2 + \delta cos(\theta_{G,i})^2}$$

where $\delta cos(\theta_{E,G,i})$ are the uncertainties in the calculation of the scattering angles. Geometrically, the uncertainty in calculation is due to spatial resolution limitations, whereas using Compton kinematics, the uncertainty in calculation is due to energy resolution limitations. Therefore, a way to reduce the χ^2 statistic for any possible interaction sequence would be to reduce both the spatial and energy resolutions of the detector. In any case, the interaction with the lowest χ^2 value is taken to be the most likely sequence, and the LOR is assigned based on the first interaction within that given sequence.

Since the χ^2 value does not uniquely determine if a given interaction sequence is correct, but rather gives a probability that the sequence is correct, it is possible to devise a method for weighting LORs based on the individual probability that the correct first interaction point is

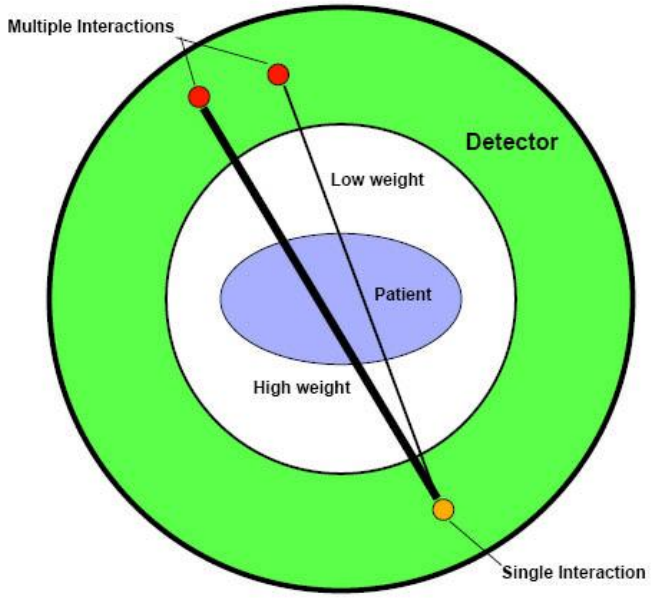

Figure 15: Representation of weights applied to multiple events within the same detector element. A high weight would manifest as more counts in the LOR reconstructed.

identified. A weighting method based on χ^2 would serve to emphasize the most probable LORs while minimizing noise contributions from the more ambiguous sequences. It has been found that certain sequences such as the 2-2 and 1-2 events can have as much as 50% ambiguity in the order of interactions based on χ^2 statistics, particularly when there are two interactions of approximately the same energy deposition. Since these ambiguous configurations would naturally have a higher χ^2 statistic, they would tend to be minimized. However, no information would be lost from the reconstruction as with a threshold cut on χ^2 values. Therefore, a weighting scheme would serve to both retain useful information as well as minimizing noise contributions from improbable or ambiguous sequences. For each possible sequence s, a weight w_s was calculated by

$$w_s = \left[1/\chi_s{}^2\right]^x$$

where $x \epsilon (0,1)$ is the weighting exponent. The weighting exponent is an arbitrary value that can be optimized for either fast computation or large reduction in noise contributions (see next section). The weighting method is to multiply the LORs by the weight in both the list mode and sinogram outputs, thus increasing the relative importance of sequences with a low χ^2 value. Furthermore, LORs can be added to the outputs for the sequences that were not the most probable, according to the relative χ^2 value of the sequence.

$$\begin{array}{rr} (x_1,y_1,z_1) \xrightarrow{w_1} \begin{matrix}(x_1,y_1,z_1)\\(x_1,y_1,z_1)\end{matrix} & (r_1,\theta_1,\varphi_1) \xrightarrow{w_1} \begin{matrix}(r_1,\theta_1,\varphi_1)\\(r_1,\theta_1,\varphi_1)\end{matrix} \\ (x_2,y_2,z_2) \xrightarrow{w_2} \begin{matrix}(x_2,y_2,z_2)\\(x_2,y_2,z_2)\\(x_2,y_2,z_2)\end{matrix} & (r_2,\theta_2,\varphi_2) \xrightarrow{w_2} \begin{matrix}(r_2,\theta_2,\varphi_2)\\(r_2,\theta_2,\varphi_2)\\(r_2,\theta_2,\varphi_2)\end{matrix} \end{array}$$

In this study, we compared the effects of including LOR information from both the first and second most probable interaction sequences while discarding all others.

Noise Reduction Evaluation

Two methods were used to evaluate the effects of the Compton weighting scheme on overall image quality: evaluation of scatter fraction (SF) according to NEMA standards, and image reconstruction of list mode data using an iterative maximum likelihood expectation maximum

(MLEM) algorithm. In both cases, simulations were performed using the rat-like and mouse-like phantoms following NEMA protocol. The list mode MLEM reconstruction was developed by A. Andreyev (see (25)).

Scatter Fraction – NEMA Standard

The calculation of scatter fraction using the NEMA standard proceeded as in (25). For both the rat-like and mouse-like phantoms, 25 million 18F decay events were simulated. The weighted sinogram output oblique angles (φ) were rebinned into 2-dimensional projections (containing r, θ, z) with 1 cm slices in the z direction using the SSRB method. A bin width of 0.3 mm was applied to the radial data r, and any radial bins that were greater than 8 mm from the edge of each phantom were discarded. Then, for each projection angle θ, the radial values were shifted so that the maximum value was aligned with the central pixel of the sinogram (in this case the $r = 0$ value). Then, for each angular projection i, the re-aligned pixels were summed according to the radial projection. The number of pixels between -7mm and +7mm from the central maximum were multiplied by the average of the summed pixel values at $\pm$7mm to obtain an intermediate value p_i. To find the average pixel values, linear interpolation was used. This intermediate value p_i was then added to the number of counts outside the central 14mm region and divided by the number of pixels outside the region to obtain the scattered event count $C_{s,i}$. The total event count $C_{T,i}$ was obtained by dividing the sum of all pixel values in the projection by the number of pixels. The scatter fraction (SF) was then given by dividing the scattered counts by the total counts and summing over all axial slices

$$SF = \sum_{i=1}^{N} C_{s,i} \Big/ C_{T,i}$$

where N is the total number of slices. The scatter fraction was calculated for sinograms generated from the normal χ^2 threshold method, and weighting methods for various weighting exponents, and compared to the correct LOR data from the Geant4 simulated points with blurring only due to the detector response as outlined in the previous section.

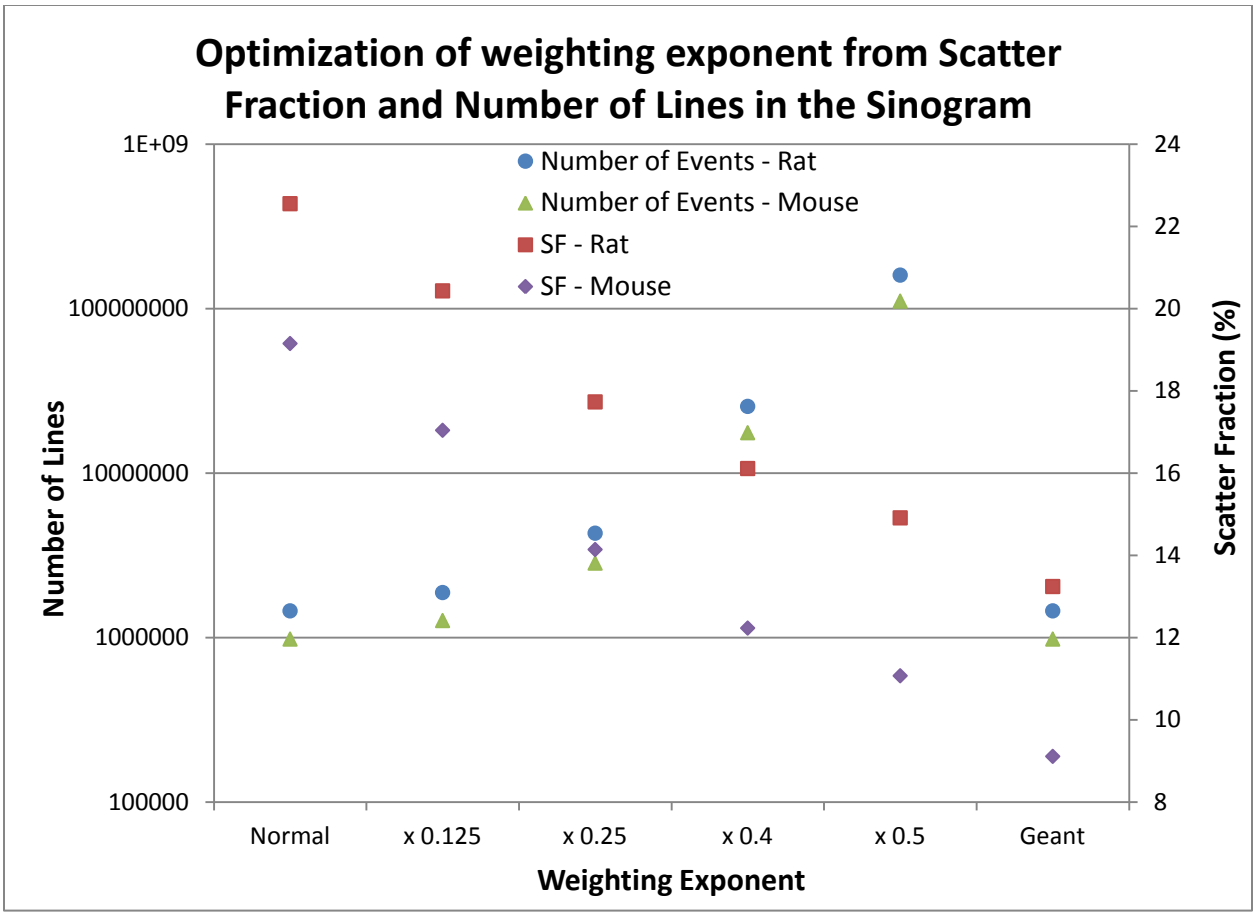

Figure 16: Reduction in scatter fraction with an increase in the weighting exponent. The increase in weighting exponent has a dramatic effect on the number of LORs that are included in the image reconstruction. Optimization would depend on computing time and noise reduction requirements.

	Rat-Like Phantom		Mouse-Like Phantom	
Weighting Value	**Scatter Fraction**	**Number of Lines**	**Scatter Fraction**	**Number of Lines**
None (Threshold)	22.55	1452454	19.15	1447802
X=0.125	20.43	1876729	17.04	1862653
X=0.250	17.73	4307579	14.14	4239845
X=0.400	16.11	25421611	12.23	24918734
X=0.500	14.91	159719341	11.07	150647882
True Geant4 Data	13.24	1452454	9.11	1447802

Table 7: Reduction in scatter fraction for various weighting exponents. The reduction has the opposing effect of a significant increase in the number of LORs used in the image reconstruction, which increases the computing time dramatically.

MLEM Reconstruction

Reconstructed images of both the rat-like and mouse-like phantoms were performed using the list mode MLEM reconstruction code. The maximum likelihood expectation maximum algorithm is an iterative method that alternates between calculating the likelihood of a given measurement (the expectation) and calculating parameters based on maximizing the expected measurement (the maximization) (30).

Reconstructions were performed using a pixel size of 0.3 mm with an image size of 180x180 pixels and 180 axial slices. Images were optimized with 50 iterations for both phantoms. To analyze the effect of the Compton weighting scheme, a weighting exponent of 0.25 was chosen because of a suitable trade-off between reduction in scatter fraction and increase in the computation time due to increase in the number of LORs to reconstruct. The weighted image was compared to reconstructed images using the normal thresholding scheme and the true LORs from simulated data.

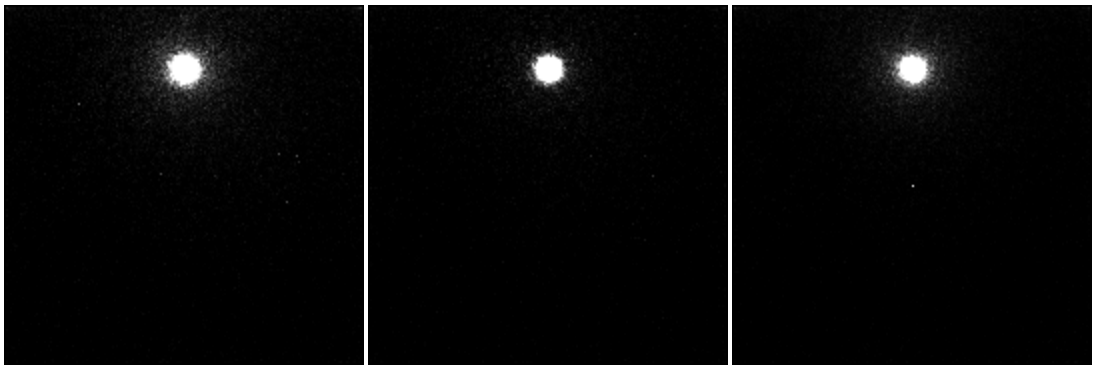

Figure 17: Reconstructed image of the Rat-Like NEMA standard phantom using list-mode MLEM code. Image represents a single slice through the center of the source for the normal thresholding technique (left), the true Geant4 data (center) and the Compton Weighting scheme (right).

Figure 18: Reconstructed images of the mouse-like NEMA phantom using the list-mode MLEM code. Images represent the normal threshold method (left), the true Geant4 data (center), and the Compton weighting scheme (right). Reduction in scatter directly surrounding the source is apparent in the weighting method image.

To reduce noise from statistics, pixel values for each of the 180 slices were summed into a composite image representing an axial projection of the phantom into a single slice. Pixel values were then summed along the vertical direction, resulting in a histogram along the horizontal direction which represented a projection of the phantom both axially and vertically. The histogram values for the three separate images were compared for both phantoms.

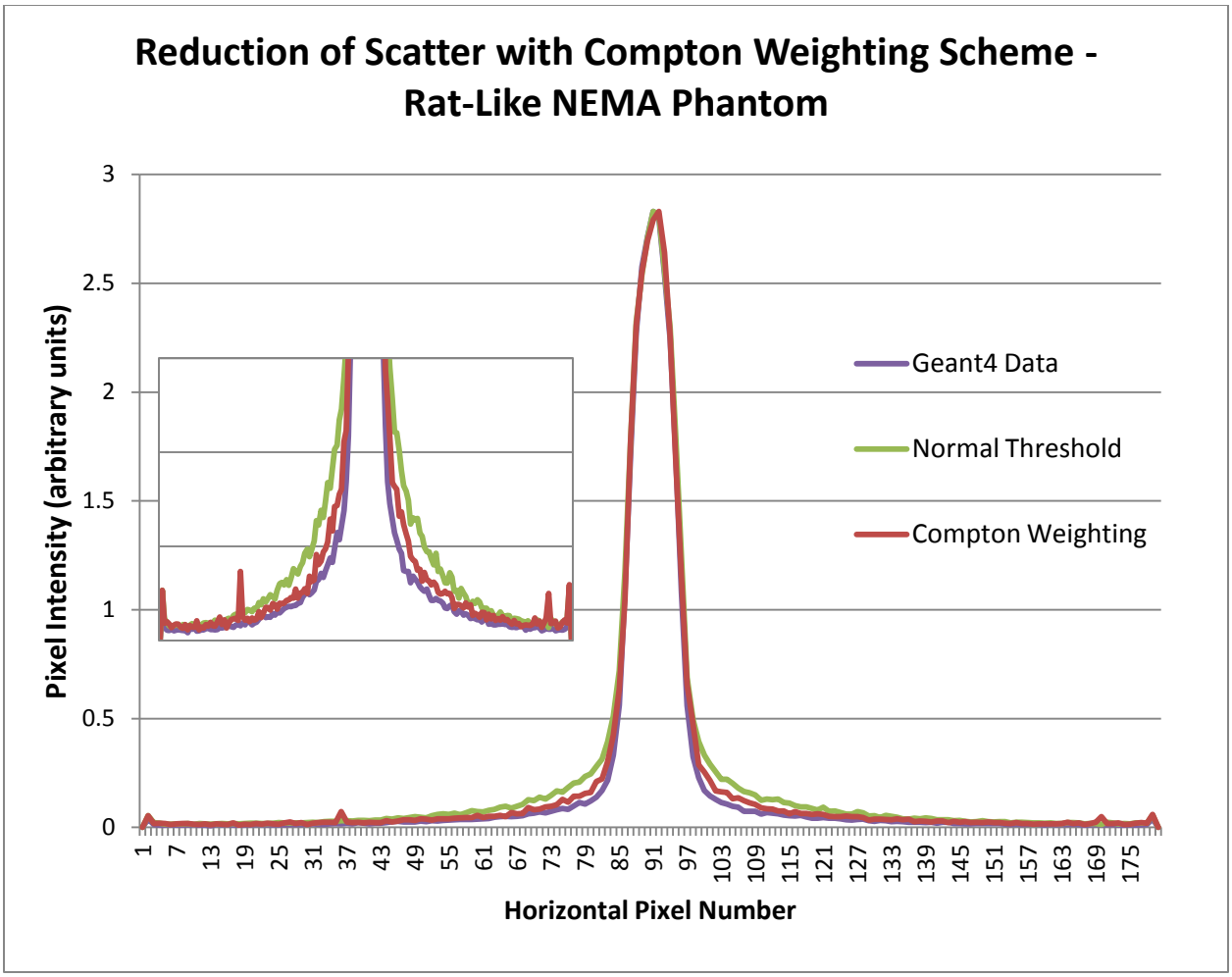

Figure 19: Histogram of the sum of axial slices and vertical pixels for the Rat-Like NEMA standard phantom. Inset graph shows pixel intensity ranges from 0 to 0.3 over the whole horizontal range of the image. The reduction in scatter contribution to the reconstructed image is visible. The Geant4 data histogram represents the theoretical minimum scatter contribution for the system.

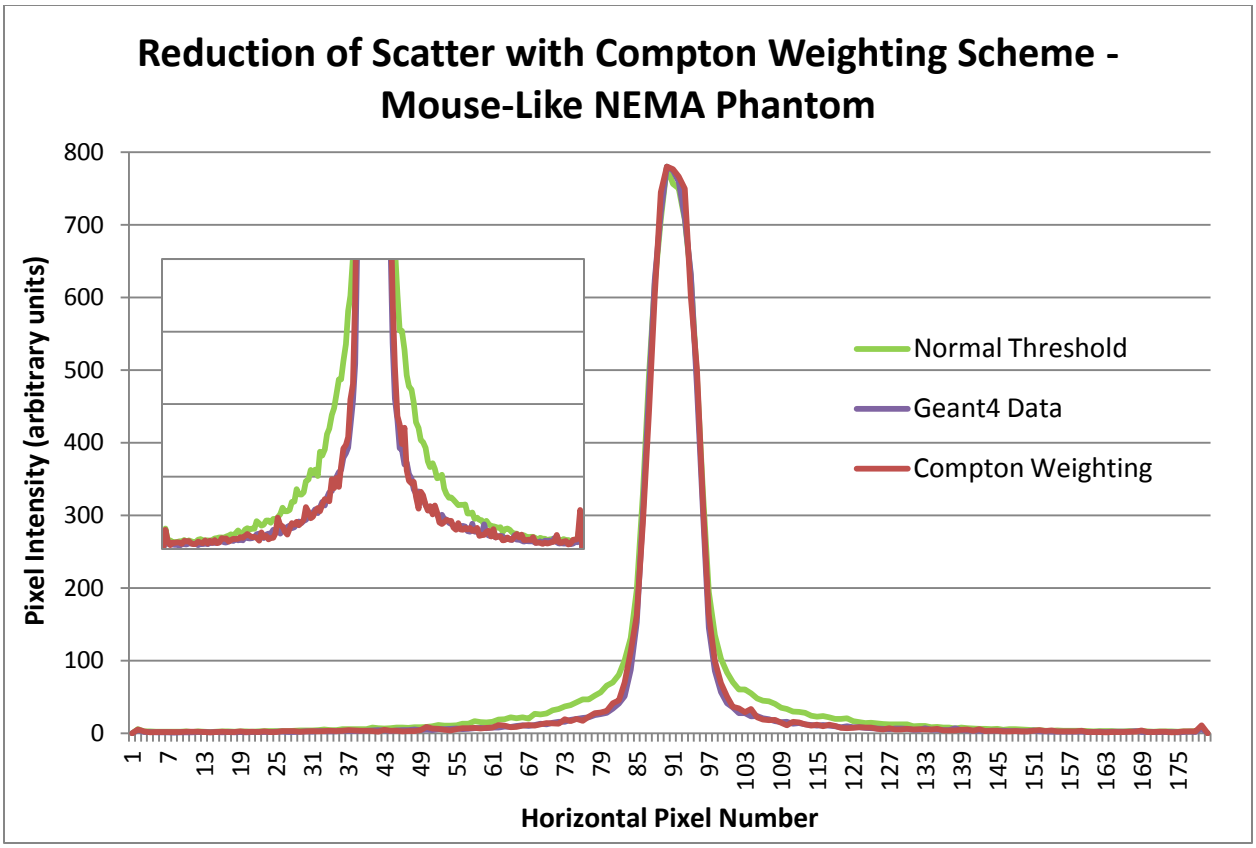

Figure 8: Histogram of the sum of axial slices and vertical pixels for the Mouse-Like NEMA standard phantom. Inset graph shows pixel intensity ranges from 0 to 80 over the whole horizontal range of the image. In this case the reduction in scatter comes close to the maximum reduction possible as represented by the Geant4 data reconstruction.

The results of the Compton weighting scheme indicate that a significant reduction in scatter contributions is achieved even with a modest increase in number of LORs reconstructed. The position and FWHM of the central peak (the location of the source) remain relatively unchanged, however, noise contributions from mis-reconstructed LORs outside the central peak are diminished. The theoretical minimum noise contribution from scatter is represented by the reconstructed Geant4 data, which is due primarily to blurring from the detector response.

Improvements to Weighting Scheme

The Compton weighting scheme used in this study served to significantly reduce the blurring contributions due to multiple scatter events within the LXePET prototype. This reduction however came at a cost of potentially significant increases in computing time. It is expected that the main cause of the reduction was the minimization of contributions to noise due to mis-identifying the correct LOR, since most mis-identified sequences have a higher χ^2 value and thus would contribute substantially less LORs to the final image. The method devised was also rudimentary, and it is expected that further study and other methods of calculating weights could improve the effects seen in this study.

One of the most significant ways to improve this method would be in the way in which images are currently reconstructed. In essence, the reconstructed image is divided into 3-dimensional voxels, which have values that are incremented when a LOR passes through them. The accumulation of voxel values from LORs defines the source location, since no information is available as to where along the LOR the source originated from, unless time-of-flight information is obtained (see (4)). The current method works by repeatedly incrementing the same voxel values based on the number of repeated LORs in the data, which is proportional to the weight used. Since optimization is also applied to images in most reconstruction techniques, the computation time is increased by a factor greater than the increase in the number of lines added to the data set, which as seen from the weighting results, can be significant. If however, instead of incrementing multiple times due to multiple LORs, a reconstruction method that took into account the specific weight of the LOR and incremented the voxel values according to the weight, the same noise reduction could be obtained with the same number of lines in the data set.

$$\begin{matrix}(x_1,y_1,z_1)\\(x_1,y_1,z_1)\\(x_2,y_2,z_2)\\(x_2,y_2,z_2)\\(x_2,y_2,z_2)\end{matrix} \Rightarrow \begin{matrix}(x_1,y_1,z_1,w_1)\\(x_2,y_2,z_2,w_2)\end{matrix} \quad \begin{matrix}(r_1,\theta_1,\varphi_1)\\(r_1,\theta_1,\varphi_1)\\(r_2,\theta_2,\varphi_2)\\(r_2,\theta_2,\varphi_2)\\(r_2,\theta_2,\varphi_2)\end{matrix} \Rightarrow \begin{matrix}(r_1,\theta_1,\varphi_1,w_1)\\(r_2,\theta_2,\varphi_2,w_2)\end{matrix}$$

This would require modifying the image reconstruction code to accept weights and allow for increments in voxel values of less than one, however, this is beyond the scope of the current work.

Chapter 5: Conclusion

A high resolution micro-PET system based on liquid xenon time projection chambers is currently under development. Simulations of the performance of the system allow for a greater understanding of its capabilities, and provide a framework for the construction of the prototype. This work, Monte-Carlo simulations of scintillation light in single sectors of the prototype, as well as simulations of the full prototype in reconstructing images of NEMA standard phantoms were carried out in order to investigate the ability to reconstruct interaction positions using light data as well as to investigate the effects of a Compton weighting scheme on noise contributions due to scatter.

The single sector prototype simulations allowed us to use the signal from the LAAPDs to determine the interaction locations of annihilation photons within the sector using a Neural Network algorithm. With no reflective surfaces added to the inner walls of the sector and electronics noise typical to what is achievable in the prototype (~700 e-), it was found that the NN algorithm was capable of reconstructing interaction positions to within approximately 7 mm, 11 mm, and 9 mm FWHM in the X, Y, and Z directions respectively using light signals alone. When reflective surfaces were added to the inner walls of the sector, the reconstruction remained roughly constant at approximately 7 mm, 10 mm, and 8 mm FWHM in the X, Y, and Z directions respectively. In addition, an increase in electronics noise added to the LAAPD signal caused increases in the resolution of the reconstructed point. High resolution reconstruction of the interaction positions using fast light signals will greatly reduce effects of pile-up and enhance the use of the ionization signals which ultimately give sub-mm resolution.

Simulations of 18F decays in NEMA standard phantoms positioned at the center of the full ring prototype allowed for the testing of a novel Compton weighting scheme used in image reconstruction and calculation of scatter fraction. The weighting method used significantly decreased calculated scatter fraction for both the Rat-like and Mouse-like NEMA standard phantoms; however, the current method caused an increase in computing time due to the repetition of LORs used in the method. Reconstructed images showed the reduction in scatter contributions using this method, and in the case of the Mouse-like phantom, scatter was reduced to nearly the minimum amount as seen by the reconstructed Geant4 data.

In conclusion, this thesis showed that reconstruction of scintillation positions using a Neural Network algorithm was a feasible approach for the LXePET prototype for both the cases of non-reflective and reflective surfaces added to the inner walls of the sector. For cases of reflective and non-reflective surfaces on the inner walls of the chamber, the NN was able to reconstruct scintillation positions to within approximately 10 mm FWHM. This work also showed that a weighting scheme based on probability of interaction sequence for Compton scattered events within the detector could significantly reduce noise contributions from scattered events. Continued research and implementation of an image reconstruction algorithm tailored to this approach could also eliminate the negative effects of increased computation time that this method showed.

Bibliography

1. *Event-Driven Motion Compensation in Positron Emission Tomography: Development of a Clinically Applicable Method.* **Langner, Jens.** 2008, PhD Thesis - Faculty of Medicine Carl Gustav Carus, University of Technology Dresden.

2. *Calculation of positron range and its effect on the fundamental limit of positron emission tomography system spatial resolution.* **C.S. Levin, E.J. Hoffman.** 1999, Phys. Med. Biol, Vol. 44.

3. *Quantitative imaging of coronary blood flow.* **A.M. Allessio, E. Butterworth, J.H. Caldwell, J.B. Bassingthwaighte.** 2010, Nano Reviews, Vol. 1.

4. *Time-of-flight PET.* **Lewellen, T.K.** 3, 1998, Seminars in Nuclear Medicine, Vol. 28.

5. *Performance figure and images from the Therascan 3128 positron emission tomograph.* **B.E. Cooke, A.C. Evans, E.O. Fanthome, R. Alarie, A.M. Sendyk.** 1, IEEE Trans. Nucl. Sci., Vol. 31.

6. *"Quantitation in Positron Emission Computed Tomography: 7. A technique to reduce noise in accidental coincidence measurements and coincidence efficiency calibration.* **M.E. Casey, E.J. Hoffman.** J. Comput. Assist. Tomogr, Vol. 10.

7. *Patient Weight–Based Acquisition Protocols to Optimize18F-FDG PET/CT Image Quality.* **A. Nagaki, M. Onoguchi, N. Matsutomo.** 2, 2011, J. Nucl. Med. Technol., Vol. 39.

8. **Saha, Gopal B.** *Basics of PET Imaging: Physics, Chemistry, and Regulations.* s.l. : Springer, 2010.

9. *Ultrahigh-Resolution L(Y)SO Detectors Using PMT-Quadrant-Sharing for Human & Animal PET Cameras.* **R.A. Ramirez, S. Kim, Y. Zhang, S. Liu, H. Baghaei, H. Li, Y. Wang, J. Liu, W-H. Wong.** 2006, IEEE Nucl. Sci. Symp. Conf. R. 1-4244-0561-0/06.

10. *Medical imaging process accelerated in FPGA 82X faster than software.* **Z. Chen, A.W.Y. Su, M-T. Sun, S. Hauck.** 2011, EE Times.

11. **al, E. Aprile et.** *Noble Gas Detectors.* Berlin : Wiley-VCH, 2006. ISBN-10: 3-527-40957-6.

12. *XENON: A 1 Tonne Liquid Xenon Experiment For A Sensitive Dark Matter Search.* **E. Aprile, E.A. Baltz, A. Curioni, K-L. Giboni, C.J. Hailey, L. Hui, M. Kobayashi, K. Ni.** 2002, arXiv:astro-ph/0207670v1.

13. *Observation of Two-Neutrino Double-Beta Decay in Xe-136 with EXO-200.* **al, N. Ackerman et.** 2011, arXiv:1108.4193v1 [nucl-ex].

14. *A new liquid xenon scintillation detector for positron emission tomo-graph.* **Chepel, V.Y.** 1993, Nucl. Tracks Radiat. Meas. , Vol. 21.

15. *Liquid Xenon Detectors for Positron Emission Tomography.* **A. Miceli, P. Amaudruz, F. Bernard, D.A. Bryman, L. Kurchaninov, J.P. Martin, A. Muennich, F. Retiere, T.J. Ruth, V. Sossi, A.J. Stoessl.** 2011, Journal of Physics: Conference Series, Vol. In Press.

16. *Simultaneous reconstruction of scintillation light and ionization charge produced by 511 keV photons in liquid xenon: potential application to PET.* **P. Amaudruz, D. Bryman, L. Kurchaninov, P. Lu, C. Marshall, J.P. Martin, A. Muennich, F. Retiere, A. Sher.** 2009, Nucl. Instr. Meth. A, Vol. 607.

17. *Observation of Anti-correlation between Scintillation and Ionization for MeV Gamma-Rays in Liquid Xenon.* **E. Aprile, K.L. Giboni, P. Majewski, K. Ni, M. Yamashita.** 2007, arXiv0704.1118A.

18. http://geant4.cern.ch/. [Online]

19. http://root.cern.ch/. [Online]

20. http://root.cern.ch/root/html/TMultiLayerPerceptron.html. [Online]

21. **National Electronics Manufacturers Association.** *NEMA Standards Publication NU4-2008: Performance Measurements of Small Animal Positron Emission Tomographs.* Rosslyn, VA : s.n., 2008.

22. **Hebb, Donald.** *The Organization of Behavior.* New York : Wiley, 1949.

23. **Vanderplaats, G.N.** *Numerical Optimization Techniques for Engineering Design.* New York : McGraw Hill, 1984.

24. *Detection of Scintillation Light of Liquid Xenon with a LAAPD.* **V.N. Solovov, A. Hitachi, V. Chepel, M.I. Lopes, R.F. Marques, A.J.P.L. Policarpo.** 3, 2002, Nucl. Inst. Meth. Phys. Research. A, Vol. 488.

25. *Simulations of a micro-PET System based on Liquid Xenon.* **A. Miceli, J. Glister, A. Andreyev, D. Bryman, L. Kurchaninov, P. Lu, A. Muennich, F. Retiere, V. Sossi.** 2011, Phys. Med. Biol., Vol. In Press.

26. *Exact and Approximate Rebinning Algorithms for 3D PET Data.* **M. Defrise, P.E. Kinahan, D.W. Townsend, C. Michel, M. Sibomana, D.F. Newport.** 2, 1997, IEEE Trans. Med. Imaging, Vol. 16.

27. *Event Reconstruction in high resolution Compton telescopes.* **S.E. Boggs, P. Jean.** 2000, arXiv:astro-ph/0005250, Vol. 1.

28. *Performance of the Light Trigger System in the Liquid Xenon g-Ray Imaging Telescope LXeGRIT.* **U.G. Oberlack, E. Aprile, A. Curioni, K.L. Giboni.** 4, 2001, IEEE Trans. Nucl. Sci., Vol. 48.

29. *Über die Streuung von Strahlung durch freie Elektronen nach der neuen relativistischen Quantendynamik von Dirac.* **O. Klein, Y. Nishina.** 11-12, 1929, Z. F. Phys., Vol. 52.

30. *Maximum Likelihood Reconstruction in Positron Emission Tomography.* **L.A. Shepp, Y. Vardi.** 2, 1982, IEEE Trans. Med. Imaging, Vol. 1.

31. *Observation of anticorrelation between scintillation and ionization for MeV gamma rays in liquid xenon.* **E. Aprile, K.L. Giboni, P. Majewski, K. Ni, M. Yamashita.** 2007, Phys. Rev. B, Vol. 76.